

## Hydraulic fracture propagation: analytical solutions versus Lattice simulations

E. Bakhshi<sup>1</sup>, V. Rasouli<sup>2</sup>, A. Ghorbani<sup>1\*</sup> and M. Fatehi Marji<sup>1</sup>

1. Department of Mining and Metallurgical Engineering, Yazd University, Yazd, Iran  
2. Department of Petroleum Engineering, University of North Dakota, USA

Received 22 November 2018; received in revised form 22 January 2019; accepted 5 February 2019

### Keywords

Hydraulic Fracturing  
Propagation

Lattice

Numerical Simulations

Analytical Solutions

### Abstract

In this work, we used a grain-based numerical model based on the concept of lattice. The modelling was done to simulate the lab experiments carried out on the mortar samples. Also the analytical solutions corresponding to the viscosity-dominated regime were used to estimate the fracture length and width, and the results obtained were compared with the numerical simulations. As the analytical solutions are proposed for a penny-shaped fracture with no presence of any obstacle such as natural interfaces, in this work, we presented the results of lattice simulations for hydraulic fracturing in the cement sample, similar to the lab, but with no natural fractures, and compared the results obtained with analytical solutions. The results indicated that in the case of a continuous medium, the analytical solutions may present a reasonable estimation of the fracture geometry. Also the viscosity-dominated leak-off model showed a better match between the analytical solutions and the numerical simulation results, confirmed by observing fluid loss into the sample in the lab post-experiment. In the case of assuming leak-off, the results indicated that the fracture width and length would reduce. However, it should be noted that in real cases, rock formations exhibit fractures and inhomogeneity at different scales so that the applications of the analytical solutions are limited.

### Nomenclature

$u_i^t$	Velocity of component $i$
$u_i^t$	Position of component $i$
$t$	Time
$m$	Mass
$\sum F_i^{(t)}$	Sum of all force-components
$\Delta t$	Time step
$\omega_i^{(t)}$	Angular velocity of component $i$
$\sum M_i^{(t)}$	Sum of all moment-components
$I$	Interia
$\dot{u}_i^N$	Velocity of component $i$ in the normal direction
$\dot{u}_i^S$	Velocity of component $i$ in the shear direction
$n_i$	Unit normal vector
$F_i^N$	Normal spring force
$F_i^S$	Shear spring force
$k^N$	Normal stiffness of the spring
$k^S$	Shear stiffness of the spring

$g$	Gap
$\beta$	Dimensionless parameter
$k_r$	Relative permeability
$a$	Hydraulic aperture
$\mu$	Fluid viscosity
$p$	Fluid pressure
$z$	Node elevation
$\rho_w$	Fluid density
$\Delta P$	Pressure increment
$\Delta t$	Time step
$Q$	Sum of all flow rates, $q_i$
$V$	Volume of fluid element
$K_f$	Apparent fluid element bulk modulus
$E$	Rock Young's modulus
$\nu$	Poisson's ratio
$K_{IC}$	Toughness
$\Omega$	Dimensionless crack opening or aperture
$\rho$	Dimensionless scalar coordinate
$g$	Leak-off rate
$C_L$	Carter's leak-off coefficient
$V_L$	Leaked volume
$S_0$	Spurt-loss coefficient
$r_w$	Wellbore radius

## 1. Introduction

Hydraulic fracturing is a commonly used stimulation technique to improve the recovery of hydrocarbons from tight reservoirs. Many studies have been conducted regarding hydraulic fracturing initiation and propagation. These studies range from analytical calculations to lab experimental attempts, extended to numerical simulations and field testing. The latter approach has limited implications due to the large efforts and costs involved in any field operations [1-14]. Laboratory tests, where the user can control different parameters and study the impact of one, appear to be a promising approach. Test parameters such as fracturing fluid properties, fluid injection rate, and principal stresses can be controlled with great precision in the lab experimental studies. However, similar to the field tests, laboratory experiments are expensive, and doing accurate experiments to represent large field scale operations in the lab requires a great amount of effort [11, 15-19]. Despite development of several analytical models, they often fail to represent the real complex field scale situation; however, they are useful in terms of doing some preliminary designs in the absence of adequate data and information.

Several numerical simulation models including those based on continuum (e.g. finite element methods) and dis-continuum models (e.g. distinct element methods) have been proposed by different researchers [20-30].

The higher order displacement discontinuity method (HODDM) using special crack tip elements has been widely used to study the crack propagation mechanism in rocks [31-33]. These numerical techniques are also used to study the crack propagation mechanism in hydraulic fracturing [34-39]. Other studies have used different softwares such as ABAQUS, which is based upon the extended finite element method (XFEM) [40]. The discrete element method (DEM) such as the versatile particle flow codes in two dimensions (PFC2D) [19, 41] and in three dimensions (PFC3D) [42] are also used to simulate the propagation of hydraulic fracture. All of these models, except those that are based on the concept of granular material, fail to predict the real fracture geometry, which is a function of stress anisotropy and formation inhomogeneity. Therefore, they consider a pre-defined plane for the geometry of the fracture, which is less likely to be observed in real field conditions.

Lattice numerical simulation, which is based on the physics of granular material, in a new method that was implemented in this work. As the rock is simulated as a combination of grains, the lattice models are a better representative of oil- and gas-bearing formations. This method was used in this work to simulate hydraulic fracturing propagation corresponding to some lab scale experiments carried out by other researchers [43], and the results obtained were compared with the analytical solutions. We used the XSite software, a new generation tool that has been developed by the Itasca Consulting Group that has used the Bonded Particle Model (BPM) [44] and the Synthetic Rock Mass (SRM) concept [45] for simulating hydraulic fracture propagation. The current work is the continuation of this study by the authors who also use the lattice simulations for modelling the hydraulic fracture interaction with natural interfaces [46].

**2. Lattice simulation**

XSite, the new 3D program, is based on a "lattice" representation of brittle rock. A lattice consisting of point masses (nodes) connected by springs replaces the balls and contacts (respectively) of PFC3D [45].

**2.1. Mechanical model**

The lattice used in XSite is a quasi-random assembly of nodes connected by non-linear springs. The lattice code uses an explicit solution scheme for simulating non-linear behaviors. The law of motion for translational degrees of freedom consists of the following central difference formulae for each node based on Equation (1):

$$\dot{u}_i^{(t+\Delta t/2)} = \dot{u}_i^{(t-\Delta t/2)} + \sum F_i^{(t)} \Delta t / m \tag{1}$$

$$u_i^{(t+\Delta t)} = u_i^{(t)} + \dot{u}_i^{(t+\Delta t/2)} \Delta t$$

Where  $\dot{u}_i^t$  and  $u_i^t$  are, respectively, the velocity and position of component  $i$  ( $i = 1, 3$ ) at time  $t$ , and  $\sum F_i^{(t)}$  is the sum of all the force-components  $i$  acting on the node of mass  $m$  with time step  $\Delta t$  [45]. The angular velocities of component  $i$  at time  $t$  are calculated using Equation (2):

$$\omega_i^{(t+\Delta t/2)} = \omega_i^{(t-\Delta t/2)} + \frac{\sum M_i^{(t)}}{I} \Delta t \tag{2}$$

where  $\omega_i^{(t)}$  is the angular velocity of component  $i$  ( $i = 1, 3$ ) at time  $t$ , and  $\sum M_i^{(t)}$  is the sum of all moment-components  $i$  acting on the node of moment of inertia,  $I$ . After all nodes have been visited [applying Equation (1) to each one], a scan of all springs is performed. If a spring is unbroken, the following calculation is performed at time  $t$ .

$$\dot{u}_i^{rel} = \dot{u}_i^A - \dot{u}_i^B \tag{3}$$

where the superscript "rel" denotes "relative", and "A" and "B" denote the two nodes connected by the spring.

$$\dot{u}_i^N = \dot{u}_i^{rel} n_i \tag{4}$$

$$\dot{u}_i^S = \dot{u}_i^{rel} - \dot{u}_i^N n_i$$

where  $\dot{u}_i^N$  and  $\dot{u}_i^S$  are the velocity of component  $i$  in the normal and shear direction, respectively, and  $n_i$  is the unit normal vector, and changing of force in spring is calculated using the relative displacement of the nodes based on Equation (5):

$$F_i^N \leftarrow F_i^N + \dot{u}_i^N k^N \Delta t \tag{5}$$

$$F_i^S \leftarrow F_i^S + \dot{u}_i^S k^S \Delta t$$

where  $F_i^N$  and  $F_i^S$  are the normal and shear spring forces, and  $k^N$  and  $k^S$  are the normal and shear stiffness of the spring, respectively. After calculation by Equation (5), the normal force is tested for breakage. Thus if  $F_i^N > F_i^{Nmax}$  then  $F_i^N = 0$  and  $F_i^S = 0$ . During the future calculations, the spring forces remain zero while the "gap" is positive, where gap,  $g$ , is calculated as follows:

$$g = g + \dot{u}_i^N \Delta t \tag{6}$$

As soon as the gap becomes zero, the spring calculation reverts to that of Equation (5). Thereafter, the spring separates again ( $g > 0$ ,  $F_i^N = 0$ ) when the normal force becomes greater than zero. For a spring that is part of a joint segment, the shear force is limited to the maximum frictional force when the normal force is compressive ( $F_i^N < 0$ ):

$$\text{If } \left| F_i^S \right| > \mu \left| F_i^N \right| \text{ then } F_i^S t_{F_i^S} \frac{\mu \left| F_i^N \right|}{\left| F_i^S \right|} \quad (7)$$

where  $\mu$  is the friction coefficient of the joint segment [44].

## 2.2. Flow model

XSite has the ability to simulate fluid flow in both fractures and matrix differently. In fractures, the flow is simulated using the network of fluid nodes connected by pipes, while the matrix flow uses the pore pressures stored in the springs of the solid model. Because of breaking the lattice springs, the micro-cracks are created and the code automatically creates new fluid nodes and connects them using flow pipes [45].

### 2.2.1. Flow formulation in fractures

The flow rate along a pipe, from fluid node “A” to node “B”, is estimated based on Equation (8):

$$q = \beta k_r \frac{a^3}{12\mu} \left[ p^A - p^B + \rho_w g (z^A - z^B) \right] \quad (8)$$

where  $\beta$  is a dimensionless calibration parameter and a function of fluid resolution, and pipe conductivity,  $k_r$  is the relative permeability, which is a function of saturation  $s$  (see Equation 9),  $a$  is the hydraulic aperture,  $\mu$  is the viscosity of the fluid,  $p^A$  and  $p^B$  are the fluid pressures at nodes “A” and “B”, respectively,  $z^A$  and  $z^B$  are the elevations of nodes “A” and “B”, respectively, and  $\rho_w$  is the fluid density [45].

$$k_r = s^2 (3 - 2s) \quad (9)$$

The evolution of the flow model with time is solved using an explicit numerical scheme. The pressure increment  $\Delta P$  during a time step  $\Delta t_f$  is calculated based on Equation (10):

$$\Delta P = \frac{Q}{V} K_f \Delta t_f \quad (10)$$

where  $Q$  is the sum of all flow rates,  $q_i$ , from the pipes connected to the fluid element (see Equation 11),  $V$  is the volume of the fluid element, and  $K_f$  is the apparent fluid element bulk modulus [45].

$$Q = \sum_i q_i \quad (11)$$

### 2.2.2. Flow formulation in matrix

During stimulation of oil and gas reservoirs, most of the flow takes place in the induced and pre-existing fractures, leak-off into the intact rock depending on permeability of the intact rock. In XSite, the leak-off into intact rock is represented by the matrix flow. Unlike the formulation for fracture flow, which uses a separate geometry and data structure, the matrix flow is solved using the existing lattice data structure. The matrix pressure is stored at the lattice springs [45].

## 3. Scaling law

To perform a representative field experiment, the scaling laws are used to scale hydraulic fracturing parameters in laboratory. Scaling laws ensure that the hydraulic fracture is contained within the sample boundaries, and the propagation can be monitored without being affected by the boundary conditions. In fact, the scaling laws are applied to model field representative fracture growth in the laboratory by defining the fracturing parameters (e.g. viscosity) in such a way that the laboratory and field fracture propagation regimes are as similar as possible [47]. In a small-scale laboratory test considering the case of a penny-shaped fracture, it is most likely that toughness controls the fracture propagation regime at the final stage of propagation after a period of specific time. However, almost all of the field scale hydraulic fractures over nearly all of their propagation history are viscose-dominated [48]. Considering the scaling laws for the special case of a penny-shaped fracture (also referred to as a radial or axisymmetric fracture) driven by a fluid injected at a constant rate, as these laws are the key to understand the different regimes of propagation, propagation of a hydraulic fracture with zero lag is governed by two competing dissipative processes associated with fluid viscosity and solid toughness, respectively, and two competing components of the fluid balance associated with fluid storage in the fracture and fluid storage in the surrounding rock (leak-off), as described by [45]. Consequently, the limiting propagation regimes can be associated with the dominance of one of the two dissipative processes and/or the dominance of one of the two fluid storage mechanisms. Thus we can identify four primary asymptotic regimes of hydraulic fracture propagation (with zero lag), where one of the two dissipative mechanisms and one of the two fluid storage components vanish: storage-viscosity ( $M$ ), storage-toughness ( $K$ ), leak-off-viscosity ( $\tilde{M}$ ), and leak-off-toughness ( $\tilde{K}$ ) dominated regimes (Table 1).

For example, in the storage-viscosity-dominated regime (M), fluid leak-off is negligible compared to fluid storage in the fracture, and the energy expended in fracturing the rock is negligible compared to viscous dissipation. The solution in the storage-viscosity dominated limiting regime is given by the zero-toughness, zero-leak-off solution  $K' = C' = 0$  [44].

Consider the general scaling of a finite fracture that hinges on defining the dimensionless crack opening  $\Omega(\rho; p_1, p_2)$ , net pressure  $\Pi(\rho; p_1, p_2)$ ,

and fracture radius  $\gamma(\rho; p_1, p_2)$  as:

$$w = \varepsilon L \Omega, \quad p = \varepsilon E', \quad R = \gamma L \tag{12}$$

With these definitions, we have introduced the scaled coordinate  $\rho = r/R(t)$  ( $0 \leq \rho \leq 1$ ), a small parameter  $\varepsilon(t)$ , and a length scale  $L(t)$  of the same order of magnitude as the fracture length  $R(t)$ . In addition, we define two dimensionless evolution parameters  $P_1(t)$  and  $P_2(t)$ , which depend monotonically on  $t$ .

For a viscous-dominated propagation regime, the dimensionless toughness parameter of a penny-shaped fracture can be calculated using Equation (13) [48]:

$$k = K' \left( \frac{t^2}{\mu'^5 Q_0'^3 E'^{13}} \right)^{1/18} \tag{13}$$

**Table 1. The dimensionless parameters for the four asymptotic fracturing propagation regimes [44].**

Scaling	$\mathcal{E}$	$\mathcal{L}$	$\mathcal{P}_1$	$\mathcal{P}_2$
Storage/viscosity ( $M$ )	$(\frac{\mu'}{E't})^{1/3}$	$(\frac{E'Q_0'^3 t^4}{\mu'})^{1/9}$	$K_m = (\frac{K'^{18} t^2}{\mu'^5 E'^{13} Q_0'^3})^{1/18}$	$L_m = (\frac{C'^{18} E'^4 t^7}{\mu'^4 Q_0'^6})^{1/18}$
Storage/toughness ( $K$ )	$(\frac{K'^6}{E'^6 Q_0' t})^{1/5}$	$(\frac{E'Q_0' t}{K'})^{2/5}$	$M_k = (\frac{\mu'^5 Q_0'^3 E'^{13}}{K'^{18} t^2})^{1/5}$	$L_k = (\frac{C'^{10} E'^8 t^3}{k'^8 Q_0'^2})^{1/10}$
Leak-off/viscosity ( $\tilde{M}$ )	$(\frac{\mu'^4 C'^6}{E'^4 Q_0'^2 t^3})^{1/16}$	$(\frac{Q_0'^2}{C'^2})^{1/4}$	$K_{\tilde{m}} = (\frac{K'^{16} t}{E'^{12} \mu'^4 C'^2 Q_0'^2})^{1/16}$	$P_{\tilde{m}} = (\frac{\mu'^4 Q_0'^6}{E'^4 C'^{18} t^2})^{1/16}$
Leak-off/toughness ( $\tilde{K}$ )	$(\frac{\mu'^8 C'^2}{E'^8 Q_0'^2 t})^{1/8}$	$(\frac{Q_0'^2}{C'^2})^{1/4}$	$M_{\tilde{k}} = (\frac{\mu'^4 E'^{12} C'^2 Q_0'^2}{K'^{16} t})^{1/4}$	$P_{\tilde{k}} = (\frac{K'^8 Q_0'^2}{E'^8 C'^{10} t^3})^{1/8}$

where  $\mu$  is the fracturing fluid viscosity,  $E$  is the rock Young's modulus, and  $\nu$  is the Poisson's ratio. In Equation (12), the fracture propagation will be viscose-dominated if  $\kappa$  is below one, whereas it is toughness-dominated when the dimensionless toughness number exceeds four.

The evolution parameters can take either the meaning of a toughness ( $K_m, K_{\tilde{m}}$ ), or a viscosity ( $M_k, M_{\tilde{k}}$ ) or a storage ( $P_{\tilde{m}}, P_{\tilde{k}}$ ) or a leak-off coefficient ( $L_m, L_k$ ). These four solution regimes are shown in Figure 1 in a rectangular phase diagram.

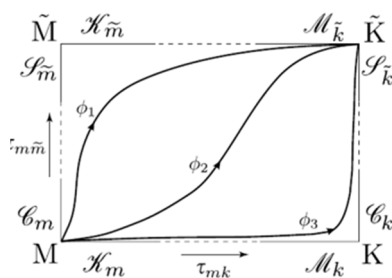


**Figure 1. The MKK̃M̃ parametric space [44].**

#### 4. Numerical simulations and design parameters

For numerical simulations, we used the geometry and input parameters of the cement samples (without any natural fractures), which were used by [43] for performing the hydraulic fracturing tests in the lab on cubical samples with sides 10 cm, and ran the XSite simulations for hydraulic fracturing. [43] prepared the cement mortar samples as a mixture of cement and water through a careful lab experimental procedure, and the minimum and maximum horizontal and vertical stresses of 1000, 2000, ~3000 psi (i.e. approximately 7, 14, and 21 MPa) were applied when testing the samples [49]. The low fracture toughness, low permeability, and low-to-moderate porosity are the key features that make the cement a good candidate for the fracturing tests. For estimating the hydro-mechanical behavior and properties of the samples, Sarmadivaleh et al. have conducted the standard hydro-mechanical tests [49]. The results of these experiments were tabulated in Table 2.

**Table 2. The hydro-mechanical properties of the cement samples and the testing methods [49].**

Hydro-mechanical property	Value	Test method
Uni-axial compressive strength, UCS psi (MPa)	11,530 ± 750 (79.5)	Unconfined compression test
Uni-axial Poisson's ratio, $\nu$	0.197 ± 0.02	Unconfined compression test
Young's modulus, $E$ , psi (GPa)	4.018 × 10 <sup>6</sup> ± 2 × 10 <sup>5</sup> (27.74)	Unconfined compression test
Internal friction coefficient, $\phi$ (degree)	44.3	Mohr circle, confined test
Cohesion, $C_c$ psi (MPa)	2524 (17.3)	Mohr circle, confined test
Tensile strength, $T_0$ , psi (MPa)	510 ± 200 (3.5)	Brazilian tensile test
Fracture toughness, $K_{IC}$ , psi $\sqrt{\text{in}}$ (MPa $\sqrt{\text{m}}$ )	710 ± 200 (0.78)	CSB
Porosity, $\phi$ %	14.7 ± 1	Two Boyle's cells
Permeability, $K$ mD	0.018 ± 0.005	Transient gas flood

In the lab, in order to maintain the viscosity-dominated fracture propagation regime, the flow rate was extremely low (1 cc/min or  $1.67 \times 10^{-8}$  m<sup>3</sup>/s), and the viscosity of the fracturing fluid was very high (97.7 Pa.s), nearly 100,000 times larger than the viscosity of water (0.001 Pa.s). Using these figures for simulations will take a very long time, which may not be feasible. Therefore, here, we simulated larger size samples, while maintaining the propagation of the fracture within the viscosity dominated regime. To do this, we multiplied the size of the lab-scale sample by 50 times and simulated cubic samples with a size of 5 m (500 cm). Accordingly, among the possible flow rates and viscosities resulting in a viscosity-dominated regime, we chose a flow rate of 0.005 m<sup>3</sup>/s and a viscosity of 0.001 Pa.s for the fracturing fluid. Based on Equation (13), this will result in a value for  $k = 0.57$ , which means that the fracture will propagate in the viscosity-dominated regime as  $k < 1$ .

The vertical well with a radius of 0.1 m was placed in the center of the sample. The fluid cluster with a radius of 0.25 m and a very weak starter crack was placed at the center of the wellbore with a radius of 0.30 m and an aperture of  $1 \times 10^{-5}$  m. The starter crack was aligned in the  $y$  direction, perpendicular to the min stress, helping the induced fracture to initiate in this direction. In the lab, commonly, a notch is created along this direction to facilitate the fracture to initiate, and this was practiced in the lab experiments done on the cement samples. It is important to note that the fracture aperture and pressure values within the starter crack zone do not represent the real values of the induced fracture opening and pressure as the starter crack has a much larger initial aperture than the rock matrix represented by the pipes. Therefore, the data within this zone is not included in the interpretation and is discarded from the plots. In practice, in the field, the near wellbore zone is a damaged zone and the fracture geometry and its

orientation are not dictated by the far field stresses, so a similar concept is used in the simulations.

The magnitudes of stresses were chosen as 1, 2, and 3 MPa in the X, Y, and Z directions. These are the same ratios to the stresses applied in the lab (i.e. 7, 14, and 21 MPa). Smaller magnitudes were chosen to initiate the fracture at lower injection pressures and assist with the computational time.

Figure 2 shows the geometry of the hydraulic fracture after 1.0 s of simulation. Due to the homogeneity of the rock and existence of no natural interface, the fracture propagates symmetrically and perpendicular to the direction of minimum stress. The fracture geometry is penny-shaped, as expected in a viscosity-dominated regime.

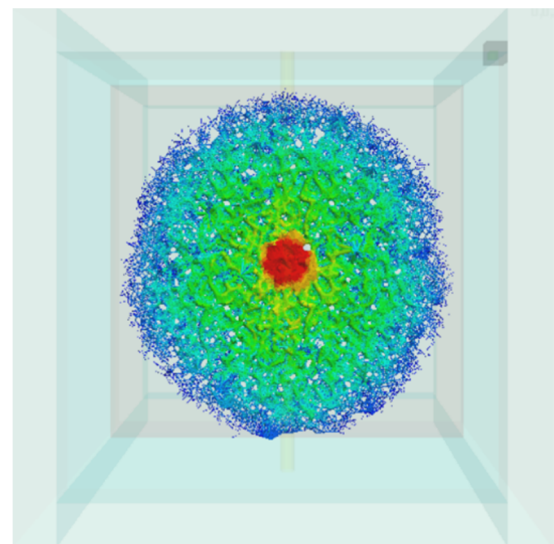
**Figure 2. Hydraulic fracture propagation after 1.0 s of simulation.**

Figure 3 (top) shows the contours of aperture and pressure in the XZ plane after 1.0 s of simulations, which confirms the penny-shaped nature of fracture geometry. Also the profiles of aperture and pressure along the white line shown on these

contours are presented in Figure 3 (bottom). The aperture and pressure are maximum near the wellbore and reduce to nearly zero at the fracture tip. In the next section, the analytical solutions to estimate the fracture geometry will be presented, and the results obtained are compared with the numerical simulations.

### 5. Viscosity-dominated model

The lab experiments carried out by [49] have simulated hydraulic fracturing in viscosity-dominated regime as  $k = 0.57 < 1$ . As the

permeability of the cement samples used for the experiment is very low and nearly zero ( $1 \times 10^{-13} \text{ m}^2$ ), it is reasonable to assume a zero leak-off. This corresponds to the asymptotic  $M$  solution (zero toughness, zero leak-off or viscosity/storage regime) presented by Pierce and Detournay [44]; also see Table 1.

The formulation of the  $M$  solution to estimate the fracture length and aperture as well as the fracture pressure during the propagation time are summarized as below [45].

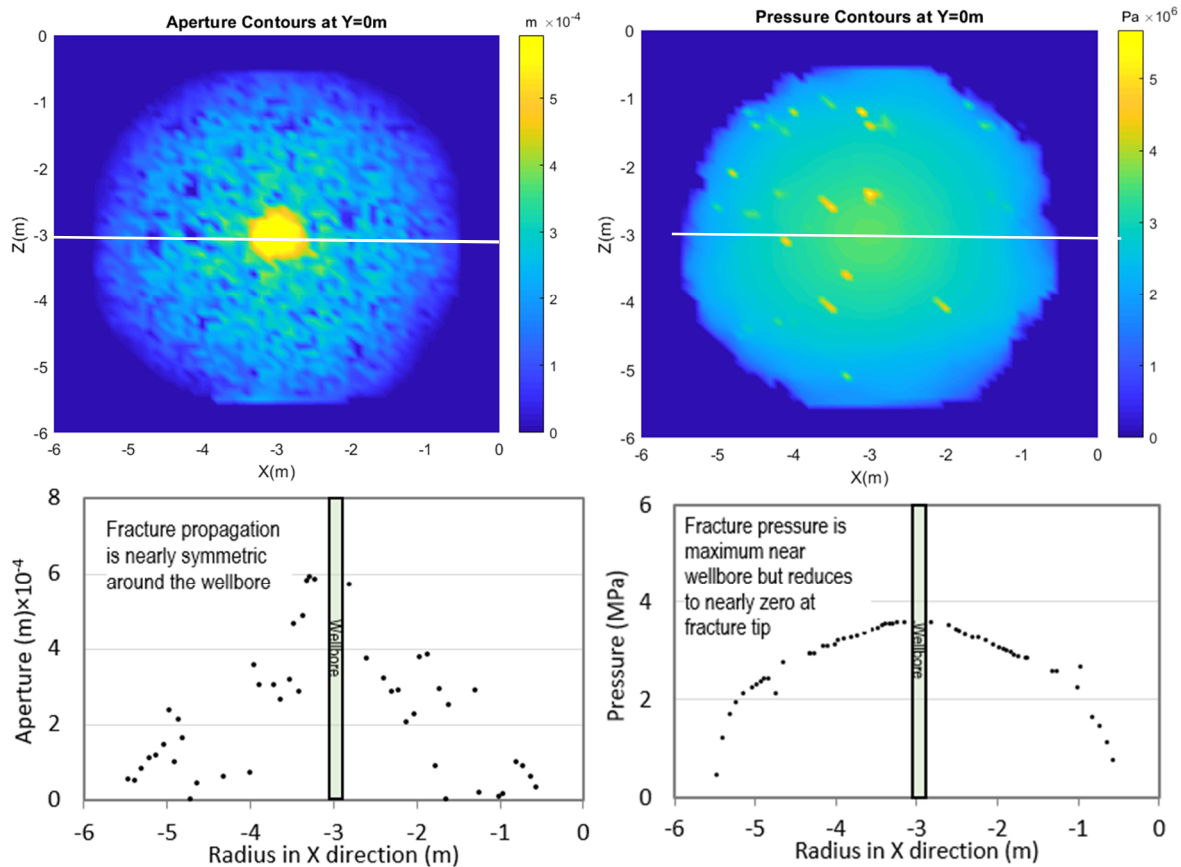


**Figure 3. Contours (top) of fracture aperture (left) and pressure (right) in the XZ plane at Y = 0 m and profiles of aperture and pressure along the white lines (bottom).**

The  $M$ -solution

$$\tau_{mo} = \{\gamma(\tau), \Omega(\rho, \tau), \Pi(\rho, \tau)\} \quad (14)$$

is given by:

$$\begin{aligned} \gamma &= \gamma_{mo} \tau^{4/9}, \\ \Omega &= \Omega_{mo}(\rho) \tau^{1/9}, \\ \Pi &= \Pi_{mo}(\rho) \tau^{-1/3} \end{aligned} \quad (15)$$

where a first-order approximation to the self-similar solution

$$\gamma_{mo}, \Omega_{mo}(\rho), \Pi_{mo}(\rho) \quad (16)$$

is given by:

$$\gamma_{mo} \approx 0.6955 \quad (17)$$

$$\begin{aligned} \Omega_{mo} &\approx (C_1 + C_{2\rho})(1 - \rho)^{2/3} \\ &\quad + B_1 [(1 - \rho^2)^{1/2} - \rho \arccos \rho] \end{aligned} \quad (18)$$

$$\begin{aligned} \Pi_{mo} &\approx A_1 \left[ \omega_1 - \frac{2}{3(1 - \rho)^{1/3}} \right] \\ &\quad - B_2 \left( \ln \frac{\rho}{2} + 1 \right) \end{aligned} \quad (19)$$

$$C_1 \approx 1.034,$$

$$C_2 \approx 0.6378,$$

$$B_1 \approx 0.1642,$$

$$A_1 \approx 0.3581,$$

$$B_2 \approx 0.09269,$$

$$\omega_1 \approx 2.479$$

The calculations of the above parameters can be easily developed in an excel spreadsheet. The plot of dimensionless crack opening or aperture ( $\Omega$ ) versus the dimensionless scalar coordinate ( $\rho$ ) is presented in Figure 4. Also shown in this figure is the plot of the dimensionless pressure ( $\Pi$ ) versus dimensionless scalar coordinate ( $\rho$ ). A quarter of the fracture geometry is plotted in Figure 4 due to the symmetric geometry of the fracture assumed by analytical calculations. In  $M$  solution, the dimensionless fracture aperture is independent from fluid viscosity. The results show the pressure changes as the fracture propagates, while the asymptotic behavior is observed at the beginning of the fracture propagation, near wellbore, and at the fracture tip when the injection stops. These results are in agreement with those presented by Savitski and Detournay [53]. The change of pressure inside the fracture is the assumption embedded in the viscosity-dominated regime.

Using the parameters of the injecting fracturing fluid presented in Section 4 (i.e.  $Q = 0.005 \text{ m}^3/\text{s}$  and  $\mu = 0.001 \text{ pa.s}$ ), the fracture aperture and pressure were calculated using the  $M$  solution after 1.0 s of simulation, and the results obtained were presented in Figure 5. In this figure, the corresponding numerical simulation results from Figure 3 are added for comparison purposes. It is to be noted that we discarded the analytical values within the 30 cm radius around the wellbore as this is the radius of the starter crack that has a large aperture to start the hydraulic fracture.

In general, there is a good agreement between the results of analytical and numerical methods for both the fracture aperture and the pressure calculations. For the viscosity-dominated regime, as one expects, the pressure inside the fracture is reduced from the maximum value near wellbore to nearly zero at the fracture tip. This trend is observed in the results shown in Figure 5. The simulation results for both the aperture and pressure data appear to deviate more from analytical solutions near the wellbore and at the fracture tip. The lack of match at small and large radial distances is due to the fact that at small distances, the numerical source is a finite volume, rather than a point source, which is assumed in the exact solution; at large distances, the finite initial aperture allows seepage, compared to zero seepage in the exact solution, which assumes zero initial aperture [45].

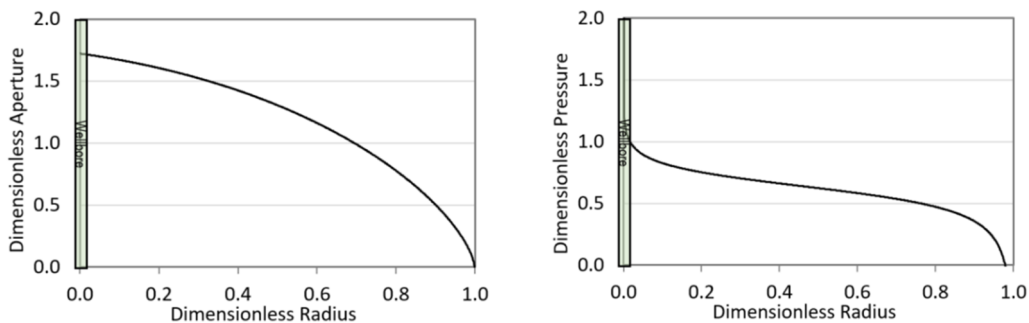


Figure 4. Dimensionless crack aperture ( $\Omega$ ) (left) versus dimensionless scalar coordinate ( $\rho$ ) (right) for  $M$  solution.

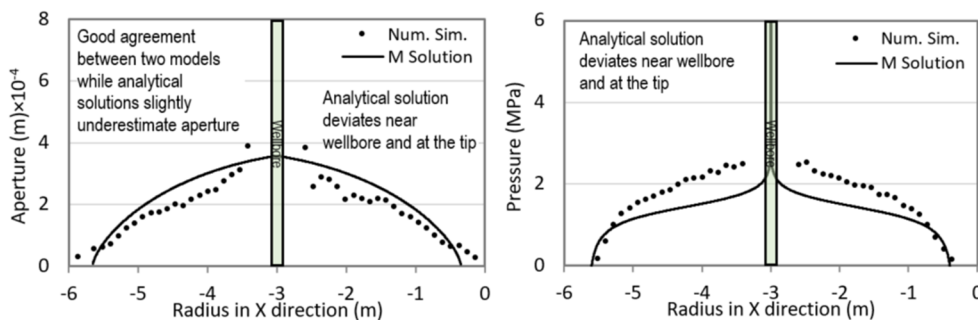


Figure 5. Fracture aperture (left) and pressure (right) versus radius after 1.0 s, numerical simulations versus  $M$  solution.

**6. Viscosity-dominated/leak-off model**

In this section, for comparison purposes, we present the results of the  $\tilde{M}$  solution corresponding to a viscosity-dominated fracture propagation in a permeable rock (viscosity-dominated/leak-off). This is assuming that the cement sample permits some invasion of the fracturing fluid into the rock matrix. The reason for this is that the invasion of the fracturing fluid is observed in the cement samples tested in the lab. This may be justified considering the  $\tilde{M}$  solution and also running simulations in XSite by activating the leak-off module. The formulation for the  $\tilde{M}$  solution to predict the fracture length, and the width and fracture pressure are presented as what follow [46].

The  $\tilde{M}$  solution:

$$\tilde{T}_{\tilde{m}o} = \{ \gamma(\tau), \Omega(\rho, \tau), \Pi(\rho, \tau) \} \tag{20}$$

is given by:

$$\begin{aligned} \gamma &= \gamma_{\tilde{m}o} \tau^{1/4}, \\ \Omega &= \Omega_{\tilde{m}o}(\rho) \tau^{1/16}, \\ \Pi &= \Pi_{\tilde{m}o}(\rho) \tau^{-3/16} \end{aligned} \tag{21}$$

where the first-order approximation to the self-similar solution  $\gamma_{\tilde{m}o}, \Omega_{\tilde{m}o}(\rho), \Pi_{\tilde{m}o}(\rho)$  is:

$$\gamma_{\tilde{m}o} = \frac{\sqrt{2}}{\pi} \tag{22}$$

$$\begin{aligned} \Omega_{\tilde{m}o} &= D_1(1 - \rho^2)^{3/2} + \\ &D_2(\sqrt{1 - \rho^2} - \rho \arccos \rho) + \\ &D_3\sqrt{1 - \rho^2} \left[ 4 - \int_0^1 2 F_1\left(\frac{3}{8}, 1, \frac{3}{2}; (1 - \rho^2)s^2 + \rho^2\right) ds \right] \end{aligned} \tag{23}$$

$$\begin{aligned} \Pi_{\tilde{m}o} &= D_4 \left[ 4 - (1 - \rho^2)^{-3/8} \right] - \\ &D_5 \left[ 3(2\rho^2 - 1) - 1 \right] + D_6 \left[ \log\left(\frac{2}{\rho}\right) - 1 \right] \end{aligned} \tag{24}$$

$$\begin{aligned} D_1 &= 0.05159, \\ D_2 &= 0.1608, \\ B_1 &= 0.1642, \\ D_3 &= 0.2976, \\ D_4 &= 0.2596, \\ D_5 &= 0.01688, \\ D_6 &= 1403 \end{aligned} \tag{25}$$

Figure 6 shows the dimensionless fracture aperture and pressure corresponding to the  $\tilde{M}$  solution. In this figure, the same values for the  $M$  solution (see Figure 4) are presented for comparison purposes. From this figure, it can be observed that the fracture aperture is smaller for the  $\tilde{M}$  than the  $M$  solution, which is due to the leak-off assumption, as not the entire fluid injection results in propagating the fracture but some losses into the formation. Accordingly, with a smaller fracture area, the pressure will be larger for the  $\tilde{M}$  than the  $M$  solution, as it can be seen in Figure 7.

The leak-off coefficient ( $C_L$ ) incorporates the effect of fluid loss into the rock. A similar concept is used in the XSite formulations, which is based upon the Carter leak-off model [50]. This is a simple model that may not be a perfect model based on its assumptions but can be used to calibrate the results against the lab or field data. The Carter model is briefly presented here.

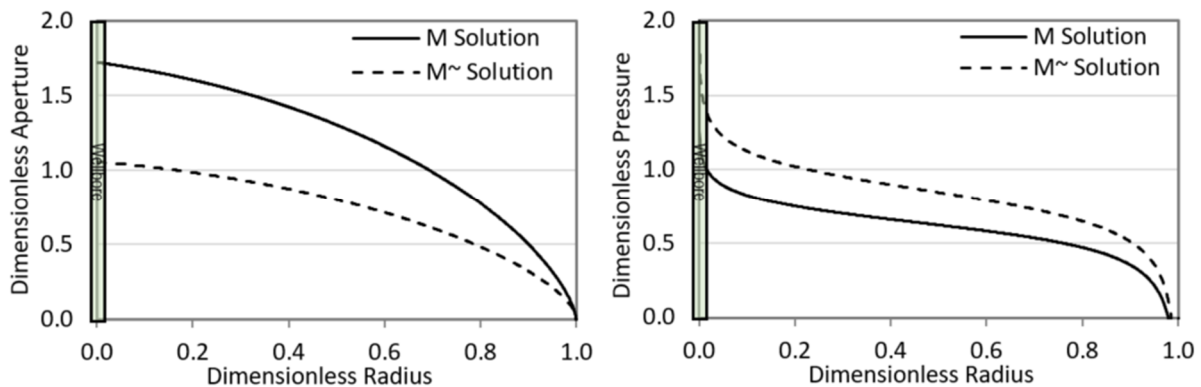


**Figure 6. Dimensionless crack aperture ( $\Omega$ ) (left) versus dimensionless scalar coordinate ( $\rho$ ) (right) for the  $\tilde{M}$  solution.**

### 6.1. Carter leak-off model

The Carter model is based on the consideration that the fracturing fluid has cake-building properties to control fluid losses. This model also relies on the assumption that the fluid loss in the formation can be approximated to a 1D flow perpendicular to the fracture faces [51]. The leak-off rate  $g$  [ $LT^{-1}$ ] is modeled using a lumped coefficient  $C_L$  [ $LT^{-1/2}$ ], known as the Carter's leak-off coefficient, and an inverse square root law on exposure time:

$$g = \frac{2C_L}{\sqrt{t-t_0}}, t > t_0 \tag{26}$$

Here, the exposure time  $t - t_0$  at a particular location on the fracture is the time elapsed between the current time  $t$  and the time  $t_0$  at which the fracture tip arrived at that location, and factor 2 comes from the consideration that the leak-off occurs on both faces of the fracture. The time integration of Equation (25) gives the fluid volume leaked per unit area of fracture (both faces counted) as:

$$\frac{V_L}{A} = 4C_L \sqrt{t-t_0} + S_0 \tag{27}$$

where  $V_L$  is the leaked volume and  $S_0$  is the spurt-loss coefficient [L]. The spurt-loss coefficient is the specific volume of fluid that infiltrates instantaneously at the beginning of the leak-off process before the filter cake (the thin low permeability barrier formed by the fracturing fluid) has time to form. The fraction of the fracturing fluid that percolates through the filter cake is called the filtrate. The thin portion of the

surrounding formation that has been invaded by the filtrate, ahead of the filter cake, is called the invaded region [51].

The coefficients  $C_L$  and  $S_0$  lump many parameters from the formation rock, fluids, and filter cake, which are, in general, difficult to measure independently. Based on the experiments performed using the rock samples with intrinsic permeability of 1 to 10 mD ( $1D = 9.81 \times 10^{-13} m^2$ ), the values reported in the literature (Constien, 1989) indicate that  $C_L$  usually varies between  $5 \times 10^{-5}$  and  $2 \times 10^{-4} m/s^{0.5}$ , and  $S_0$  change between  $4 \times 10^{-5}$  and  $7 \times 10^{-3} m$  [51].

### 6.2. Estimating cement leak-off coefficient

Due to the small size of the sample in the lab, the hydraulic fracture reaches the end of the sample in both sides and difficulty in knowing when to stop the pump after the fracture initiation point. However, what is obvious is that the fracture half length exceeded 5 cm (half sample length) after 100 s that the injection was stopped after fracture initiation time. Assuming that the fracture half length reached 7 cm, using the lab data presented in Table 2, the leak-off coefficient for the cement sample was back-calculated from the  $\tilde{M}$  solution. This resulted in a value of  $C_L = 3 \times 10^{-6} m/s^{0.5}$ . Figure 7 shows the fracture aperture and pressure versus length for the lab scale sample estimated based on the  $M$  and  $\tilde{M}$  solutions, respectively. From this figure, it can be seen that the  $\tilde{M}$  solution results in a less fracture aperture and length than the  $M$  solution with a larger fracture pressure, as one can expect.

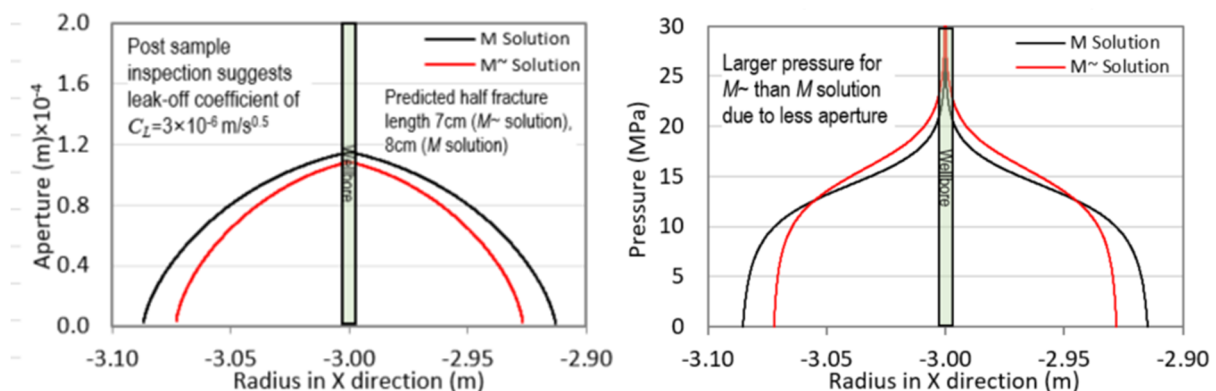


Figure 7. Fracture aperture (left) and pressure (right) versus length predicted for lab-scale cement sample of 10 cm using  $M$  (black) and  $\tilde{M}$  solution (red).

### 6.3. Numerical simulations

In order to simulate the viscosity-dominated/leak-off case numerically at large-scale, the leak-off coefficient is required to be upscaled, as it was done for the fluid viscosity and flow rate. Here, we used the dimensionless leak-off parameter proposed by [47] as:

$$N_L = C_L \sqrt{\frac{r_w}{Q}} \quad (28)$$

In this equation,  $r_w$  is the wellbore radius and  $Q$  is the flow rate. For a hydraulic fracturing experiment to correspond to a field scale operation,  $N_L$  should remain the same. Using the lab scale data ( $C_L = 3 \times 10^{-6} \text{ m/s}^{0.5}$ ,  $r_w = 0.06 \text{ in.} = 0.0015 \text{ m}$ , and  $Q = 1.67 \times 10^{-8} \text{ m}^3/\text{s}$ ), the value for the dimensionless leak-off parameter is calculated as  $N_L = 9 \times 10^{-4}$ . Considering this value and

substituting the values of  $r_w = 0.15 \text{ m}$  and  $Q = 1.0 \times 10^{-3} \text{ m}^3/\text{s}$ , which were used for the numerical simulations previously, the upscaled leak-off coefficient is calculated as  $C_L = 75 \times 10^{-6} \text{ m/s}^{0.5}$ ; this is nearly 25 times larger than that for the lab-scale leak-off coefficient, indicating the larger volume of fluid being lost into the formation in large-scale model than the lab-scale experiments. Figure 8 presents the results of numerical simulations of Figure 3 for a penny-shaped hydraulic fracture together with the corresponding  $M$  and  $\tilde{M}$  solutions (Figure 6) for comparison purposes. The leak-off numerical model assumed a leak-off coefficient of  $C_L = 75 \times 10^{-6} \text{ m/s}^{0.5}$ . The results of numerical simulation and the  $\tilde{M}$  solution for the leak-off model present a closer agreement than the model with no leak-off.

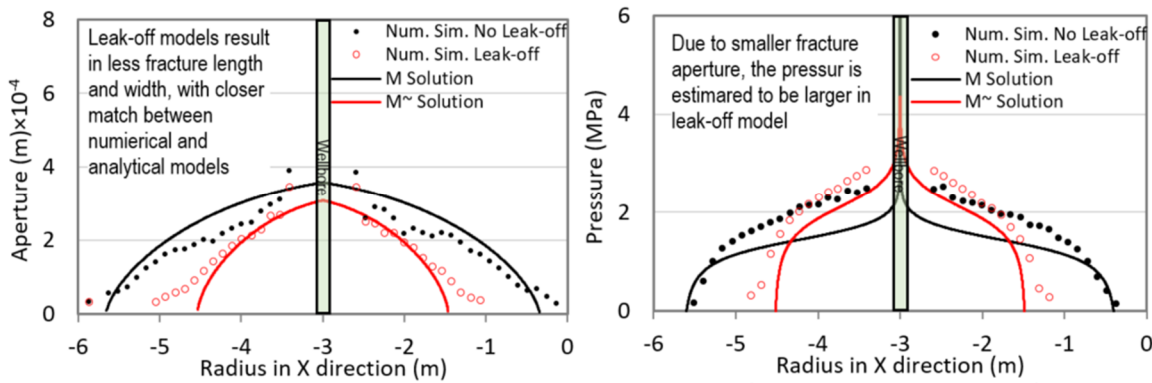


Figure 8. Fracture aperture (left) and pressure (right) estimated numerically and analytically for models with and without leak-off.

### 7. Discussion

The results obtained indicate that the analytical solutions are applicable to some very simple and specific cases. For example, for prediction of fracture geometry, it only applies to penny-shaped fractures, and the equations are based on many simplified assumptions that are not applicable to a real field. The existence of small- to large-scale fractures and rock inhomogeneity add complexity in fracture propagation, where the analytical solutions fail to present a reasonable prediction of fracture geometry. Fractures with different scales may add more complexity to the overall interaction mechanism. For example, when the hydraulic fracture arrives at a weak interface with the expectation to be arrested, if the interface is of small size, the hydraulic fracture will continue its propagation when extends to the sides of the interface.

As mentioned earlier, analytical solutions are for similar cases. However, in practice, the planes

maybe at any dip angle and orientation. Extension of the existing analytical equation to include the dip angle of natural interface will add more complexity, and may not be necessary. The numerical simulations can analyze different cases. Considering several fractures with various scales, one can recognize the difficulty in predicting the preferred fracture propagation (PFP) direction. In the real field situation, where a number of models have been proposed to simulate the distribution on fractures using discrete fracture network (DFN) [52] and analytical solutions are not suitable for these complicated cases, numerical simulations can be used in these complex fracture geometry. These limitations suggest that while the use of analytical solutions may be useful to obtain some fundamental knowledge about the fracture geometry and the parameters involved in the interaction modes, in the real field applications, they are unable to provide practical solutions. The use of numerical simulation will be of great

advantage in the real field situations, as it can analyze complex scenarios, where multiple natural fracture sets with various properties, geometry, and sizes are expected to exist. However, the key point is that the numerical simulator has adequately been validated against the lab and real field data and so the results are reliable.

## 8. Conclusions

Maintaining the same fracture propagation regime (i.e. toughness- or viscosity-dominated) when simulating lab-scale hydraulic fracture is important, the viscosity-dominated regime, similar to the lab work, was assumed. The shape of the fracture propagation was observed to be penny-shaped, which is expected in the viscosity-dominated regime. It was seen that assuming leak-off in the samples tested in the lab, it may be possible to obtain a closer match between the analytical solutions and the numerical simulation results. Also in case of assuming leak-off, the results indicate that the fracture width and length will reduce due to the fact that some of the fracturing fluid energy is lost into the formation instead of being utilized to propagate the fracture. Moreover, it was seen that the analytical solutions could not be used to predict the geometry of induced fracture in a fractured media as the existence of natural interfaces would deviate the fracture propagation path from its initial direction. This requires numerical simulations, integrating the geometry of fracture network in the model as close as possible to the real field, which is not an easy task. Finally, due to the complex fracture geometry of the real field, analytical solutions are not suitable for these complicated cases but numerical simulations, especially lattice simulation, can be used in these complex fracture geometry.

## Acknowledgments

The authors gratefully acknowledge the support of the Itasca Consulting Group for provision of the XSite license and also the valuable technical input from Dr. Branko Damjanac.

## References

[1]. Barree, R. and Mukherjee, H. (1996). Determination of pressure dependent leakoff and its effect on fracture geometry. Paper presented at the SPE Annual Technical Conference and Exhibition.

[2]. Branagan, P., Peterson, R., Warpinski, N. and Wright, T. (1996). Characterization of a remotely intersected set of hydraulic fractures: results of

intersection well no. 1-B, GRI/DOE multi-site project. Paper presented at the SPE Annual Technical Conference and Exhibition.

[3]. Daneshy, A.A. (1974). Hydraulic fracture propagation in the presence of planes of weakness. Paper presented at the SPE European Spring Meeting.

[4]. Fast, R., Murer, A. and Timmer, R. (1994). Description and analysis of cored hydraulic fractures, Lost Hills field, Kern County, California. SPE Production & Facilities. 9 (02): 107-114.

[5]. Gale, J.F., Reed, R.M. and Holder, J. (2007). Natural fractures in the Barnett Shale and their importance for hydraulic fracture treatments. AAPG bulletin. 91 (4): 603-622.

[6]. Hopkins, C., Frantz Jr, J., Hill, D. and Zamora, F. (1995). Estimating fracture geometry in the naturally fractured Antrim Shale. Paper presented at the SPE Annual Technical Conference and Exhibition.

[7]. Jeffrey, R., Enever, J., Phillips, R., Moelle, D. and Davidson, S. (1992). Hydraulic fracturing experiments in vertical boreholes in the German Creek Coal seam.

[8]. Jeffrey, R., Settari, A. (1995). A comparison of hydraulic fracture field experiments, including mineback geometry data, with numerical fracture model simulations. Paper presented at the SPE Annual Technical Conference and Exhibition.

[9]. Kaufman, P.B., Penny, G.S. and Paktinat, J. (2008). Critical evaluation of additives used in shale slickwater fracs. Paper presented at the SPE Shale Gas Production Conference.

[10]. Pursley, J.T., Penny, G.S., Benton, J.H., Greene, D.T., Nordlander, G.S., McDougall, M.A. and Crafton, J.W. (2007). Field case studies of completion fluids to enhance oil and gas production in depleted unconventional reservoirs. Paper presented at the Rocky Mountain Oil & Gas Technology Symposium.

[11]. Renshaw, C. and Pollard, D. (1995). An experimentally verified criterion for propagation across unbounded frictional interfaces in brittle, linear elastic materials. Paper presented at the International journal of rock mechanics and mining sciences & geomechanics abstracts.

[12]. Rodgerson, J.L. (2000). Impact of natural fractures in hydraulic fracturing of tight gas sands. Paper presented at the SPE Permian basin oil and gas recovery conference.

[13]. Warpinski, N., Branagan, P., Peterson, R. and Wolhart, S. (1998). An interpretation of M-site hydraulic fracture diagnostic results. Paper presented at the SPE Rocky Mountain Regional/Low-permeability Reservoirs Symposium.

[14]. Warpinski, N., Lorenz, J., Branagan, P., Myal, F. and Gall, B. (1993). Examination of a Cored Hydraulic Fracture in a Deep Gas Well (includes associated

papers 26302 and 26946). SPE Production & Facilities. 8 (03): 150-158.

[15]. Blair, S., Thorpe, R. and Heuze, F. (1990). Propagation of fluid-driven fractures in jointed rock. Part 2- physical tests on blocks with an interface or lens. Paper presented at the International Journal of Rock Mechanics and Mining Sciences & Geomechanics Abstracts.

[16]. Blair, S.C., Thorpe, R.K., Heuze, F. and Shaffer, R. (1989). Laboratory observations of the effect of geologic discontinuities on hydrofracture propagation. Paper presented at the The 30<sup>th</sup> US Symposium on Rock Mechanics (USRMS).

[17]. Rasouli, V. (2012). Hydraulic fracturing for in situ stress measurements-a simulation and experimental study. Australian Centre for Geomechanics. pp. 239-246.

[18]. Rasouli, V., Sarmadivaleh, M. and Nabipour, A. (2011). Some challenges in hydraulic fracturing of tight gas reservoirs: an experimental study. The APPEA Journal. 51 (1): 499-506.

[19]. Sarmadivaleh, M., Rasouli, V. and Ramses, W. (2011). Numerical simulations of hydraulic fracture intersecting an interbed of sandstone. Harmonising Rock Engineering and the Environment. 455 P.

[20]. Abdollahipour, A., Marji, M.F., Bafghi, A.Y. and Gholamnejad, J. (2016). DEM simulation of confining pressure effects on crack opening displacement in hydraulic fracturing. International Journal of Mining Science and Technology. 26 (4): 557-561.

[21]. Damjanac, B. and Cundall, P. (2016). Application of distinct element methods to simulation of hydraulic fracturing in naturally fractured reservoirs. Computers and Geotechnics. 71: 283-294.

[22]. Ingraffea, A.R. and Heuze, F.E. (1980). Finite element models for rock fracture mechanics. International Journal for Numerical and Analytical Methods in Geomechanics. 4 (1): 25-43.

[23]. Marji, M.F. (2014). Numerical analysis of quasi-static crack branching in brittle solids by a modified displacement discontinuity method. International Journal of Solids and Structures. 51 (9): 1716-1736.

[24]. Marji, M.F. (2015). Simulation of crack coalescence mechanism underneath single and double disc cutters by higher order displacement discontinuity method. Journal of Central South University. 22 (3): 1045-1054.

[25]. Moës, N., Dolbow, J. and Belytschko, T. (1999). A finite element method for crack growth without remeshing. International journal for numerical methods in engineering. 46 (1): 131-150.

[26]. Stevens, D.J. and Krauthammer, T. (1988). A finite difference/finite element approach to dynamic

soil-structure interaction modelling. Computers & structures. 29 (2): 199-205.

[27]. Wu, K., Olson, J., Balhoff, M.T. and Yu, W. (2017). Numerical analysis for promoting uniform development of simultaneous multiple-fracture propagation in horizontal wells. SPE production & operations. 32 (01): 41-50.

[28]. Xing, P., Yoshioka, K., Adachi, J., El-Fayoumi, A., Damjanac, B. and Bungler, A.P. (2018). Lattice simulation of laboratory hydraulic fracture containment in layered reservoirs. Computers and Geotechnics. 100: 62-75.

[29]. Zeng, Q.-D., Yao, J. and Shao, J. (2018). Numerical study of hydraulic fracture propagation accounting for rock anisotropy. Journal of Petroleum Science and Engineering. 160: 422-432.

[30]. Zhang, X., Jeffrey, R.G. and Thiercelin, M. (2007). Deflection and propagation of fluid-driven fractures at frictional bedding interfaces: a numerical investigation. Journal of Structural Geology. 29 (3): 396-410.

[31]. Haeri, H., Shahriar, K., Marji, M. and Moarefvand, P. (2014). Investigation of fracturing process of rock-like Brazilian disks containing three parallel cracks under compressive line loading. Strength of Materials. 46 (3): 404-416.

[32]. Hosseini Nasab, H. and Fatehi Marji, M. (2007). A semi-infinite higher-order displacement discontinuity method and its application to the quasistatic analysis of radial cracks produced by blasting. Journal of Mechanics of Materials and Structures. 2 (3): 439-458.

[33]. Marji, M.F., Hosseini-Nasab, H. and Kohsary, A.H. (2007). A new cubic element formulation of the displacement discontinuity method using three special crack tip elements for crack analysis. JP J. Solids Struct. 1 (1): 61-91.

[34]. Abdollahipour, A., Marji, M.F., Bafghi, A.Y. and Gholamnejad, J. (2015). Simulating the propagation of hydraulic fractures from a circular wellbore using the Displacement Discontinuity Method. International Journal of Rock Mechanics and Mining Sciences. 80: 281-291.

[35]. Behnia, M., Goshtasbi, K., Marji, M.F. and Golshani, A. (2014). Numerical simulation of crack propagation in layered formations. Arabian Journal of Geosciences. 7 (7): 2729-2737.

[36]. Abdollahipour, A., Marji, M.F., Bafghi, A.Y. and Gholamnejad, J. (2016). Numerical investigation of effect of crack geometrical parameters on hydraulic fracturing process of hydrocarbon reservoirs. Journal of Mining and Environment. 7 (2): 205-214.

[37]. Abdollahipour, A., Marji, M.F., Bafghi, A.Y. and Gholamnejad, J. (2016). Time-dependent crack propagation in a poroelastic medium using a fully

coupled hydromechanical displacement discontinuity method. *International Journal of Fracture*. 199 (1): 71-87.

[38]. Abdollahipour, A., Marji, M.F., Bafghi, A.Y. and Gholamnejad, J. (2016). A complete formulation of an indirect boundary element method for poroelastic rocks. *Computers and Geotechnics*. 74: 15-25.

[39]. Moradi, A., Tokhmechi, B., Rasolui, V. and Marji, M.F. (2018). Displacement discontinuity analysis of the effects of various hydraulic fracturing parameters on the crack opening displacement (COD). *Journal of Petroleum Science and Technology*. 8 (3): 3-13.

[40]. Dehghan, A.N., Goshtasbi, K., Ahangari, K., Jin, Y. and Bahmani, A. (2017). 3D numerical modeling of the propagation of hydraulic fracture at its intersection with natural (pre-existing) fracture. *Rock Mechanics and Rock Engineering*. 50 (2): 367-386.

[41]. Zhou, J., Zhang, L., Braun, A. and Han, Z. (2017). Investigation of Processes of Interaction between Hydraulic and Natural Fractures by PFC Modeling Comparing against Laboratory Experiments and Analytical Models. *Energies*. 10 (7): 1001.

[42]. Potyondy, D.O. (2007). Simulating stress corrosion with a bonded-particle model for rock. *International journal of rock mechanics and mining sciences*. 44 (5): 677-691.

[43]. Sarmadivaleh, M. (2012). Experimental and numerical study of interaction of a pre-existing natural interface and an induced hydraulic fracture. (Doctor of Philosophy), Curtin University.

[44]. Peirce, A. and Detournay, E. (2008). An implicit level set method for modeling hydraulically driven fractures. *Computer Methods in Applied Mechanics and Engineering*. 197 (33-40): 2858-2885.

[45]. Damjanac, B., Detournay, C., Cundall, P., Purvance, M. and Hazzard, J. (2011). XSite-

Description of Formulation. Retrieved from ITASCA Consulting Group., Inc.

[46]. Bakhshi, E., Rasouli, V., Ghorbani, A., Marji, M.F., Damjanac, B. and Wan, X. (2018). Lattice Numerical Simulations of Lab-Scale Hydraulic Fracture and Natural Interface Interaction. *Rock Mechanics and Rock Engineering*. pp. 1-23.

[47]. de Pater, C., Cleary, M., Quinn, T., Barr, D., Johnson, D. and Weijers, L. (1994). Experimental verification of dimensional analysis for hydraulic fracturing. *SPE Production & Facilities*. 9 (04): 230-238.

[48]. Detournay, E. (2004). Propagation regimes of fluid-driven fractures in impermeable rocks. *International Journal of Geomechanics*. 4 (1): 35-45.

[49]. Sarmadivaleh, M. and Rasouli, V. (2015). Test design and sample preparation procedure for experimental investigation of hydraulic fracturing interaction modes. *Rock Mechanics Rock Engineering*. 48 (1): 93-105.

[50]. Howard, G.C. and Fast, C. (1957). Optimum fluid characteristics for fracture extension. Paper presented at the Drilling and Production Practice.

[51]. Detournay, C. (2016). Implementation of Carter leak-off in Xsite. Retrieved from tasca Consulting Group.

[52]. Dershowitz, W., Klise, K., Fox, A., Takeuchi, S. and Uchida, M. (2002). Channel Network and Discrete Fracture Network Modeling of Hydraulic Interference and Tracer Experiments and the Prediction of Phase C Experiments. SKB Report IPR-02-29. Stockholm, SKB.

[53]. Savitski, A. and Detournay, E. (2002). Propagation of a penny-shaped fluid-driven fracture in an impermeable rock: asymptotic solutions. *International Journal of Solids and Structures*. 39 (26): 6311-6337.

## انتشار هیدرولیکی شکستگی: مقایسه روش‌های تحلیلی با شبیه‌ساز لاتیس

الهام بخشی<sup>۱</sup>، وامق رسولی<sup>۲</sup>، احمد قربانی<sup>۱\*</sup> و محمد فاتحی مرجی<sup>۱</sup>

۱- دانشکده مهندسی معدن و متالورژی، دانشگاه یزد، ایران

۲- دانشکده مهندسی نفت داکوتای شمالی، آمریکا

ارسال ۲۰۱۸/۱۱/۲۲، پذیرش ۲۰۱۹/۲/۵

\* نویسنده مسئول مکاتبات: ah.ghorbani@yahoo.com

---

### چکیده:

در این پژوهش به شبیه‌سازی شکست هیدرولیکی با استفاده از لاتیس پیشرفته پرداخته شده است. برخلاف روش‌های دیگر، شبیه‌ساز لاتیس یک مدل مبتنی بر ذرات است که از روش المان مجزا (DEM) استفاده می‌کند. مدل‌سازی‌ها برای شبیه‌سازی آزمون‌های آزمایشگاهی انجام شده بر روی نمونه‌های سیمانی انجام شد. همچنین روش‌های تحلیلی مربوط به رژیم ویسکوزیته غالب برای تخمین طول و عرض شکست مورد استفاده قرار گرفت و نتایج به دست آمده با شبیه‌سازی‌های عددی مقایسه شد. از آنجایی که روش‌های تحلیلی فقط برای شکستگی‌های سکه‌ای شکل و بدون حضور هیچ‌گونه شکستگی از قبیل فصل مشترک‌های طبیعی قابل استفاده می‌باشند؛ بنابراین در این پژوهش به منظور مقایسه نتایج شبیه‌سازی‌ها با روش‌های تحلیلی، شبیه‌سازی شکست هیدرولیکی توسط لاتیس بر روی نمونه‌های سیمانی مشابه با شرایط آزمایشگاهی ولی بدون حضور شکستگی‌های طبیعی انجام شد. بررسی نتایج نشان می‌دهد که در یک محیط پیوسته، روش‌های تحلیلی ممکن است تخمین مناسبی برای هندسه شکست ارائه دهند. همچنین در مدل نشت ویسکوزیته غالب، تطابق بهتری بین روش‌های تحلیلی و نتایج شبیه‌سازی‌های عددی مشاهده شد که با مشاهده نشت سیال در نمونه‌ها در آزمون‌های آزمایشگاهی نیز تأیید شد. بررسی نتایج در حالت نشت، بیانگر کاهش عرض و طول شکستگی است. با این حال باید توجه داشت که در شرایط واقعی میدان و به دلیل وجود شکستگی‌ها و ناهمگنی‌های مختلف در نمونه‌های سنگی، استفاده از روش‌های تحلیلی محدودتر خواهد بود.

**کلمات کلیدی:** انتشار شکست هیدرولیکی، لاتیس، شبیه‌سازی‌های عددی، روش‌های تحلیلی.

---